Fine optical alignment correction of astronomical spectrographs via in-situ full-field moment-based wavefront sensing

Lee, Hanshin, Hill, Gary, Tuttle, Sarah, Vattiat, Brian

Fine Optical Alignment Correction of Astronomical Spectrograph via *In situ* Full-field Moment-based Wavefront Sensing

Hanshin Lee[1], Gary J. Hill, Sarah E. Tuttle, and Brian L. Vattiat

McDonald Observatory, University of Texas at Austin, 2515 Speedway Stop 1402, Austin, TX 78712-0259, USA

ABSTRACT

The image moment-based wavefront sensing (IWFS) utilizes moments of focus-modulated focal plane images to determine modal wavefront aberrations. This permits fast, easy, and accurate measurement of wavefront error (WFE) on any available finite-sized isolated targets across the entire focal plane (FP) of an imaging system, thereby allowing not only in-situ full-field image quality assessment, but also deterministic fine alignment correction of the imaging system. We present an experimental demonstration where fine alignment correction of a fast camera system in a fiber-fed astronomical spectrograph, called VIRUS, is accomplished by using IWFS.

Keywords: Image moment, Wavefront sensing, In situ, Full field image quality, Astronomical Spectrograph, VIRUS instrument

1. INTRODUCTION

An optical wavefront is aberrated during its passage through physical systems due to perturbations such as turbulence in the Earth's atmosphere or misalignment of a telescope. A useful understanding of the observed image quality of these systems can be obtained by sensing the aberration coefficients of the wavefront. Typically, a wavefront is measured at the pupil of an imaging system, as in Shack– Hartmann sensors (SHS), where the wavefront slope is measured and then wave aberration is determined from the measurement[1]. It can be efficient and accurate, but it requires a separate relay for pupil reimaging with additional optical components. In some cases, one wishes to sense a wavefront across the field of view of an instrument by using the built-in components without separate relay components. Such desires can be satisfied by applying focal-plane wavefront sensing (FPWFS) techniques to focus-diverse images. Curvature sensing (CS) is a FPWFS method in which the intensity difference between two extrafocal images is used to determine the wavefront[2]. The CS signal is directly related to the shape of a membrane deformable mirror, enabling efficient control of the wavefront compensator[1]. In phase retrieval, another FPWFS method, the wavefront is optimized until its synthetic focus- diverse images closely match the measured ones[3]. It can be accurate and flexible, but it may be less efficient than others due to a potentially large amount of number crunching during optimization. However, progress has been made to address this issue[4][5][6].

In this paper, we describe the idea of a new type of FPWFS technique called the image-moment based wavefront sensing (IWFS). This idea was first described in Ref. [7]. Like others FPWFS techniques, the IWFS utilizes focus-diverse point spread functions (PSFs), but differs in the way of sensing aberrations as follows. The geometric shape of a point-spread function (PSF) is in frequent use for both qualitative and quantitative assessment of image quality (IQ) of optical systems. When viewed at different focus modulations (FMs), the PSF shape changes and such variation can permit IQ-evaluators to quickly determine the types (plus rough amounts in some cases) of aberrations affecting the image without using more sophisticated devices. This is in fact equivalent to the classic Star testing. Noting that a PSF is a photon distribution, it was recognized that a PSF shape could be described by some linear combination of different image moments. Also realized was that these image moments are closely related with aberrations in the PSF and their variations across multiple FMs can be utilized to deterministically compute the aberration coefficients affecting the PSF. This permits fast, easy, and accurate measurement of wavefront error (WFE) on any available finite-sized isolated targets across the entire focal plane (FP) of an imaging system, thereby permitting not only in-situ full-field image quality assessment, but also deterministic fine alignment correction of the imaging systems. The presented geometric analysis shows that the moments are nonlinear functions of wave aberration coefficients, but we note that focus diversity (FD) essentially decouples the coefficients of interest, leading to linear equations whose solution corresponds to modal coefficient estimates. We present an experimental demonstration where fine alignment correction of a fast camera system in a fiber-fed astronomical spectrograph, called VIRUS (Visible Integral-field Replicable Unit Spectrograph)[8], is accomplished by using IWFS.

---

[1] Hanshin Lee: E-mail: lee@astro.as.utexas.edu

2. IMAGE MOMENT BASED WAVEFRONT SENSING (IWFS)

The IWFS is a new type of modal wavefront sensing technique that utilizes focal-plane images. The sensed quantities are wave aberration coefficients. Compared to the other FP-WFS, the IWFS differs in the way of utilizing the focal-plane images. The main measurement of the IWFS is the kth moment of the image of an object. If the image is considered as a 2D distribution of light, the moments simply tell us about the geometric shape of the distribution. For example, the 1st moment (i.e. centroid) corresponds to the systematic image shift, and the 2nd moment (variance) describes the systematic spread of the distribution. As the order k grows, the finer details of the distribution shape are revealed, e.g. skewness and kurtosis. Measuring moments from an image is merely a simple extension of measuring the centroid or full-width-half-maximum (FWHM) of a point spread function (PSF) and thus can permit rapid WFS.
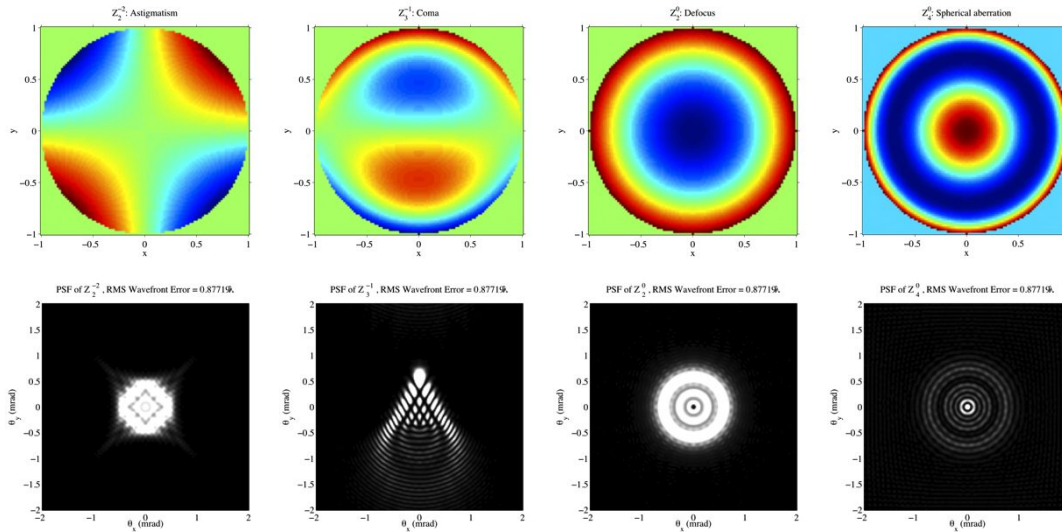
Figure 1 Example wavefront aberrations (top row) and their corresponding point spread functions (bottom row). Astigmatism, coma, defocus, and spherical aberration (from left to right).

Geometrically, a system free from aberrations focuses rays from a point object onto a point image. With non-zero wavefront aberrations, rays are spread around and a blurred image results. Each different aberration changes the image shape in a uniquely different way as in Figure 1. This means that there must be some relation between image shapes and wavefront aberrations, which we can understand by looking at how ray aberration arises from wavefront aberration. Suppose that the wavefront (Φ) from a point source at a particular field on a circular pupil, Ω, is expressed in terms of a weighted linear combination of M Zernike polynomials (Z_i) that are functions of pupil coordinates (h_x, h_y).

$$\Phi = \sum_{i=1}^{M} W_i \, Z_i(h_x, h_y), \tag{1}$$

where W_i is the i-th wave aberration coefficient. The ray coordinates (X, Y) at the focus are given by the first derivative of the wavefront with respect to the pupil coordinates.

$$X = 2F \frac{\partial \Phi}{\partial h_x} = 2F \vec{W} \, \mathbf{D} \, \vec{Z} = \vec{A}^T \, \vec{Z} \quad \text{and} \quad Y = 2F \frac{\partial \Phi}{\partial h_y} = 2F \vec{W} \, \mathbf{E} \, \vec{Z} = \vec{B}^T \, \vec{Z} \tag{2}$$

where F is the focal ratio of the system. This equation essentially defines the geometric image distribution of light for a point object. Here, we used Noll's finding that the derivatives of Z_i can be given in terms of Z_i through the conversion matrices $\mathbf{D}$ and $\mathbf{E}$[9]. When the aberration coefficient vector is multiplied to the conversion matrices, wavefront slope aberration coefficients (vectors A and B) result, whose elements are related to W_i (see Eq. 3 for example).

$$A_1 = 2W_2 + 2\sqrt{2}W_8 \qquad B_1 = 2W_3 + 2\sqrt{2}W_7$$
$$A_2 = 2\sqrt{3}W_4 + \sqrt{6}W_6 \qquad B_2 = \sqrt{5}W_5 + \sqrt{10}W_{13}$$
$$A_3 = \sqrt{5}W_5 + \sqrt{10}W_{13} \qquad B_3 = 2\sqrt{3}W_4 - \sqrt{6}W_6$$
$$A_4 = 2\sqrt{6}W_8 \qquad B_4 = 2\sqrt{6}W_7 \qquad\qquad (3)$$
$$A_5 = 2\sqrt{3}W_7 + 2\sqrt{3}W_9 \qquad B_5 = 2\sqrt{3}W_8 - 2\sqrt{3}W_{10}$$
$$A_6 = 2\sqrt{3}W_8 + 2\sqrt{3}W_{10} \qquad B_6 = -2\sqrt{3}W_7 + 2\sqrt{3}W_9$$

One way of quantifying the shape of the image distribution is to compute the kth image moment as given generally as,

$$\mu_{nm} = \frac{1}{S}\int_\Omega I\,(X - \mu_{10})^n\,(Y - \mu_{01})^m\,d\Omega, \qquad (4)$$

Here I is the pupil illumination and the 0th moment S corresponds to the total illumination. μ_{10} and μ_{01} are the 1st image moments. Apparently, μ_{nm} is non-linear in A_i and B_i for $k > 1$. However, there are terms at order k that contain $(A_2)^\alpha(B_3)^\beta$ multiplied by A_j or B_j such that $k = \alpha + \beta + 1$. As in Eq. 3, A_2 and B_3 are the only coefficients affected by defocus aberration (W_4). Therefore, the k-1th partial derivative of those terms with respect to W_4 decouples A_j or B_j from others. For example, μ_{nm} for $k=2$ are given as,

$$\mu_{20} = \sum_{i=2}^M A_i^2, \quad \mu_{11} = \sum_{i=2}^M A_i\,B_i, \quad \mu_{02} = \sum_{i=2}^M B_i^2, \qquad (5)$$

and their first derivatives with respect to W_4 are

$$\frac{\partial\mu_{20}}{\partial W_4} = 4\sqrt{3}A_2, \; \frac{\partial\mu_{11}}{\partial W_4} = 4\sqrt{3}A_3, \; \frac{\partial\mu_{02}}{\partial W_4} = 4\sqrt{3}B_3, \qquad (6)$$

We note that $A_3 = B_2$ from Eq. 3. As another example, the second partial derivatives of μ_{nm} for $k=3$ with respect to W_4 are given as the following:

$$\frac{\partial^2\mu_{30}}{\partial W_4^2} = 12\sqrt{3}(A_4 + \sqrt{2}A_6), \; \frac{\partial^2\mu_{12}}{\partial W_4^2} = 4\sqrt{3}(5A_4 - 3\sqrt{2}A_6),$$

$$\frac{\partial^2\mu_{21}}{\partial W_4^2} = 4\sqrt{3}(5B_4 + 3\sqrt{2}B_6), \; \frac{\partial^2\mu_{03}}{\partial W_4^2} = 12\sqrt{3}(B_4 - \sqrt{2}B_6), \qquad (7)$$

$$\text{with} \quad A_5 = \sqrt{2}B_4 + B_6 \; \text{and} \; B_5 = \sqrt{2}A_4 + A_6,$$

Solving the above results in the slope aberration coefficients that can be used to solve for wavefront coefficients via the relations between the wave and slope coefficients in Eq. 2. Likewise, the k-1th partial derivatives of the kth moments with respect to the wavefront defocus can be used to determine the slope aberrations and subsequently wavefront aberrations up to order k. From a practical point of view, the moment measurement is just an extension of the image centroid calculation. Thus the computation can be simple and straightforward.

Table 1 The number of focus-diversities (N) for determining aberration coefficients up to order k.

| k	N	Moments	Slope coefficients	Wave coefficients
1	1	$\mu_{1,0}\,\mu_{0,1}$	$A_1\;B_1$	$W_2\;\;W_3$
2	2	$\mu_{2,0}\,\mu_{1,1}\,\mu_{0,2}$	$A_2\;A_3\;B_2\;B_3$	$W_4\;\;W_5\;\;W_6$
3	3	$\mu_{3,0}\,\mu_{2,1}\,\mu_{1,2}\,\mu_{0,3}$	$A_4\;A_5\;A_6\;B_4\;B_5\;B_6$	$W_7\;\;W_8\;\;W_9\;\;W_{10}$
4	4	$\mu_{4,0}\,\mu_{3,1}\,\mu_{2,2}\,\mu_{1,3}\,\mu_{0,4}$	$A_7\,A_8\,A_9\,A_{10}\;\;B_7\,B_8\,B_9\,B_{10}$	$W_{11}\,W_{12}\,W_{13}\,W_{14}\,W_{15}$
5	5	$\mu_{5,0}\,\mu_{4,1}\,\mu_{3,2}\,\mu_{2,3}\,\mu_{1,4}\,\mu_{0,5}$	$A_{11}\,A_{12}\,A_{13}\,A_{14}\,A_{15}\;\;B_{11}\,B_{12}\,B_{13}\,B_{14}\,B_{15}$	$W_{16}\,W_{17}\,W_{18}\,W_{19}\,W_{20}\,W_{21}$
6	6	$\mu_{6,0}\,\mu_{5,1}\,\mu_{4,2}\,\mu_{3,3}\,\mu_{2,4}\,\mu_{1,5}\,\mu_{0,6}$	$A_{16}\,A_{17}\,A_{18}\,A_{19}\,A_{20}\;\;B_{16}\,B_{17}\,B_{18}\,B_{19}\,B_{20}$	$W_{22}\,W_{23}\,W_{24}\,W_{25}\,W_{26}\,W_{27}\,W_{28}$
7	7	$\mu_{7,0}\,\mu_{6,1}\,\mu_{5,2}\,\mu_{4,3}\,\mu_{3,4}\,\mu_{2,5}\,\mu_{1,6}\,\mu_{0,7}$	$A_{21}\,A_{22}\,A_{23}\,A_{24}\,A_{25}\,A_{26}\;\;B_{21}\,B_{22}\,B_{23}\,B_{24}\,B_{25}\,B_{26}$	$W_{29}\,W_{30}\,W_{31}\,W_{32}\,W_{33}\,W_{34}\,W_{35}\,W_{36}$

The partial derivative with respect to W4 means focus-diversity. Through-focusing a focal plane is one practical way to achieve focus-diversity. In this simplest implementation, one needs to record the image of an object at k different extra-focal planes and the amount of focus diversity is $\Delta W_4 = \Delta L/(16\sqrt{3}F^2)$ where ΔL is the amount of focal plane shift. This then allows one to express the kth moment as a function of ΔW_4. It can be fit by the kth order polynomial to

determine the partial derivatives up to order *k*-1, which are essentially the fitting coefficients. Another way of achieving focus-diversity is to use an active optical element, such as deformable mirrors or liquid crystal lenses, which is needed anyway for adaptive image compensation, for example. The focal plane can be fixed in position in such cases. The following table summarizes the number of focus-diversities for aberrations up to order *k*.

3. DISCUSSION

3.1. Brief overview of the VIRUS Instrument and HETDEX project
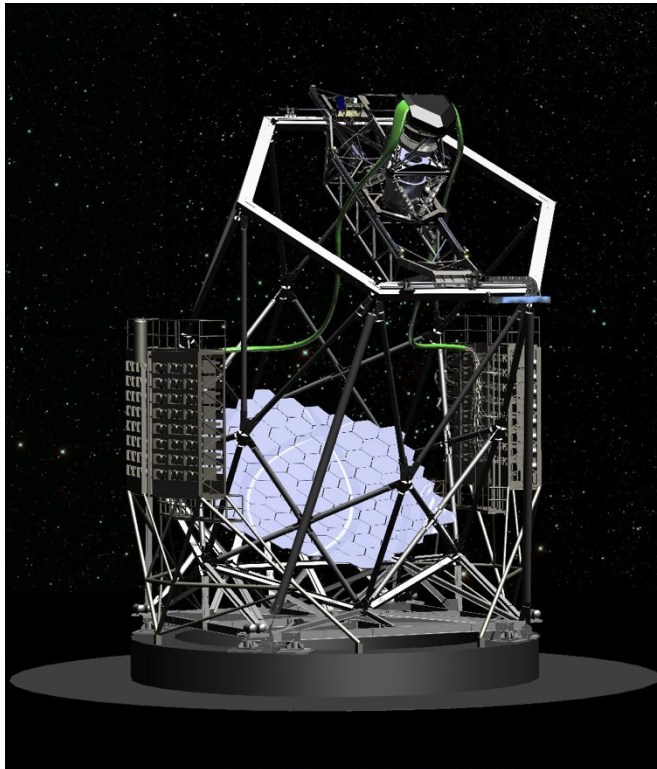
Figure 2 Rendering of the upgraded HET with the VIRUS instrument mounted on the telescope.

Before discussing the results from applying IWFS to the VIRUS instrument[8], we give a brief overview of the instrument and its purpose below. The VIRUS instrument is made up of 150+ individually compact and identical spectrographs, each fed by a fiber integration field unit. The instrument provides integral field spectroscopy from 350nm to 550nm of over 33,600 spatial elements per observation, each 1.8 sq. arc-seconds on the sky, at a spectral resolution of R ~ 700. The instrument will be fed by a new wide-field corrector (WFC) of the Hobby-Eberly Telescope[2] (HET) with increased science field of view as large as 22 arc-minutes in diameter and telescope aperture of 10m[10]. The construction of the large number of VIRUS units requires the individual spectrographs be interchangeable at sub-system level and a production line assembly process be utilized, while meeting the optical performance specification.

The main science motivation of the VIRUS instrument is to map the evolution of dark energy for the Hobby-Eberly Telescope Dark Energy Experiment (HETDEX), by observing 0.8M Lyman-α emitting galaxies as tracers. In order to achieve this science objective, we are conducting three main engineering/science projects: a major telescope upgrade including replacing the top end of the telescope to allow for a larger focal plane (Wide Field Upgrade)[10], the construction of the Visual Integral-Field Replicable Unit Spectrograph (VIRUS) instrument, and the execution of a large area (5000 square degrees) blind survey for Lyman-α emitting galaxies at redshifts z < 3.5.

The requirement to survey large areas of sky with the VIRUS instrument and the need to perform wavefront sensing for closed-loop active alignment control of the tracker position led us to design a new corrector employing meter-scale mirrors and covering a 22-arcmin diameter field of view. The HET Wide Field Upgrade (WFU) deploys this wide field corrector (WFC), a new tracker prime focus instrument package (PFIP), and new metrology systems. The new corrector has improved image quality and a 10m pupil diameter. The periphery of the field will be used for guiding and wavefront sensing to provide the necessary feedback to maintain the telescope alignment correctly. The WFC will give 30 times larger observing area than the current HET corrector. It is a four-mirror design with two concave 1 meter diameter mirrors, one concave 0.9 meter diameter mirror, and one convex 0.23 m diameter mirror. In order to feed optical fibers at f/3.65 to minimize focal ratio degradation (FRD), the WFC is designed to be telecentric at its curved focal surface so that the chief rays from all field angles are normal to the concave spherical focal surface centered at the exit pupil vertex. Due to excellent aberration correction, the imaging performance of the WFC is 0.5arcsec or better over the entire field of view with minimal obscuration across the field. The College of Optical Sciences at the University of Arizona is manufacturing the WFC[11]. A new tracker is needed to accommodate the size and four-fold weight increase of the new PFIP. It will be a third generation evolution of the trackers for HET and SALT, and is in essence a precision six-axis

---

motion control stage. The tracker is developed by the Center for Electro-Mechanics (CEM) at the University of Texas at Austin[10].

The VIRUS is based upon a novel instrument design philosophy unlike those used in traditional astronomical spectroscopic instrumentation where a monolithic single spectrograph for a large telescope with large and expensive optics and mechanisms observes the entire focal plane of the telescope. We have taken a different approach to designing the VIRUS instrument based on our concept and studies[12][13][14][15], where we concluded that industrial replication offers significant cost-advantages when compared to a traditional monolithic spectrograph, particularly in the cost of the optics and engineering effort. This concept appears to be a cost-effective approach to outfitting the existing large telescopes as well as the coming generation of ELTs, for certain instrument types, where the multiplex advantage can be used to image-slice and thus avoid growth in the scale of instruments with telescope aperture. This new approach led us to the VIRUS instrument design as follows. The entire VIRUS instrument is comprised of an array of simple, compact, inexpensive, and yet highly performing unit optical spectrographs. Each VIRUS unit samples only a small fraction of the telescope focal plane that is finely sampled by 224 fibers each covering 1.8arcsec^2 on the sky. The fibers feeding a two-unit module are packaged in a square array format that covers a 50×50arcsec^2 Integral Field Unit (IFU) with a 1/3 fill-factor. A three-exposure dither pattern fills in the gap. The optical design of the unit spectrograph is essentially based upon two Schmidt design; one as a collimator in a reversed Schmidt form and the other as a camera in a normal Schmidt design, both joined together at a common pupil plane. The optical beam train is formed by three reflections and four refractions (i.e. three mirrors and two lenses). With dielectric reflective coatings optimized for the wavelength range, high throughput is obtained. The full VIRUS array will consist of between 150 and 194 units, depending on funding, and simultaneously observe a minimum of 33,600 spectra with 12 million resolution elements. The IFUs are arrayed within the 22′ field of the upgraded HET with ~1/7 fill factor, sufficient to detect the required density of LAEs for HETDEX. Development is proceeding with the prototype (VIRUS-P), deployed in October 2006, and the production prototype where value engineering has been used to reduce the cost for production. Figure 2 shows a rendering of the upgraded telescope, showing the VIRUS mounted to the side of the telescope. The construction of the large number of VIRUS units requires the individual spectrographs be interchangeable at sub-system level and a production line assembly process be utilized, while meeting the optical performance specification. These requirements pose a strong emphasis on careful analysis of the manufacturing and alignment tolerances of the unit spectrograph design. In the following, the VIRUS unit spectrograph is briefly described. Figure 3 illustrates the optical layout of the VIRUS unit spectrograph and a sectioned view of the two-unit VIRUS module opto-mechanical model. The optical design of the unit spectrograph is comprised of two sub-systems, both based upon the Schmidt design concept utilizing a Volume Phase Holographic Grating (VPHG). In-depth discussion about the design, tolerance, and construction of the instrument can be found in Ref. [8] and [16].
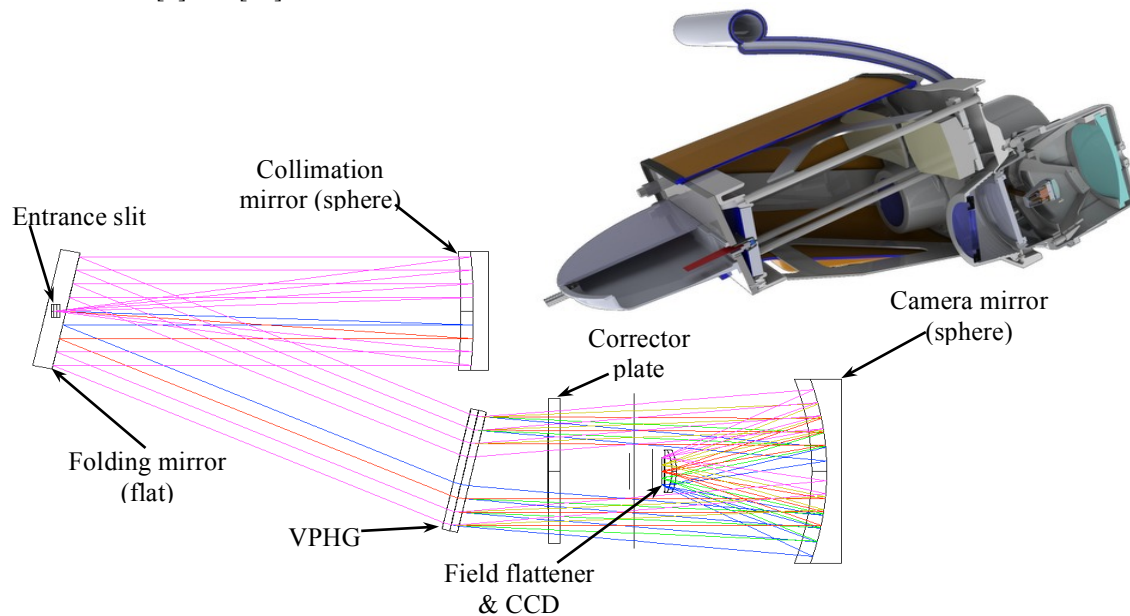
Figure 3 The optical ray trace and rendering of the VIRUS unit spectrograph.

3.2.   Fine Optical Alignment Scheme for the VIRUS Unit.

Snapshots of various parts of the VIRUS unit are shown in Figure 4. Channel A is on the left and Channel B is on the right (in A). For mechanically setting up and aligning optical components, we use a Faro Arm with the arm length of 8ft (See in B). Typical accuracy of the Faro arm is 50µm, which is sufficient for the mechanical alignment and particularly useful to check the relative alignment between the head and base plates (as shown in A). Once the mechanical alignment is completed, the system is optically aligned. For this alignment we have two alignment compensators. One of them is in the collimator. The back of the collimator mirror (in D) is glued to a disk plate that is then mounted to an Aluminum triangular plate. Each corner of this plate has a through hole within which a slit-cut spherical bearing is attached. The plate then rides on three invar rods (in E) through these bearings. Each spherical bearing has a clamping screw that can be tightened down the slit to fix the collimator mirror in position once adjustment is completed. Three springs are mounted on the invar rods pushing the plate from the front while three fine-threaded (pitch size of 0.75mm) adjuster screws pushes the plate from the back through the back plate (in A). Each collimator adjuster is separated from each other by 120degrees in azimuth angle. Tip, tilt, and focus motions can be adjusted using these screws. The main purpose of the collimator adjustment is to provide a way to center the collimated beam on the VPH gratings as shown in D. Currently the gratings are mounted to a temporary grating mount. A new adjustable cell will replace this.
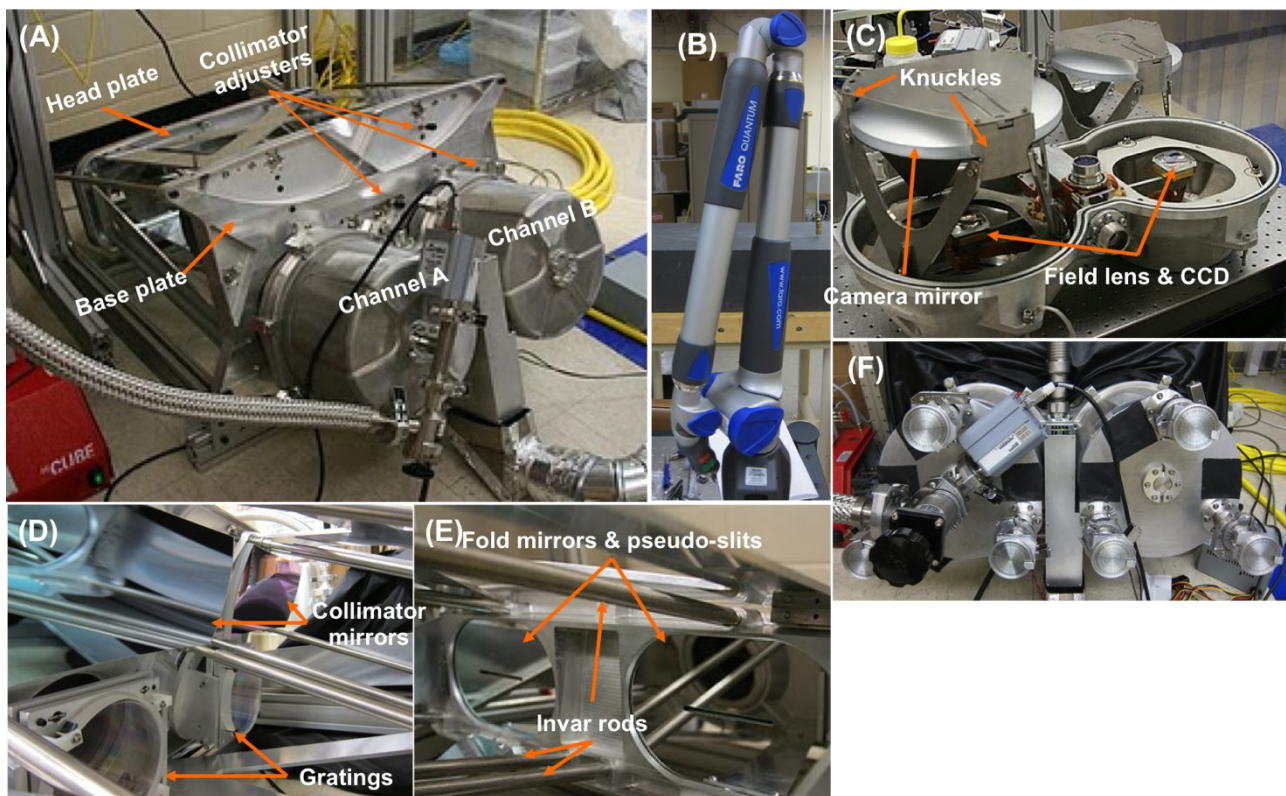
Figure 4 Snapshots of different parts of the VIRUS unit.

The other adjustment is in the camera mirror assembly (shown in C). The mirror is held from the side by three knuckle mounts (called knuckles in the figure) that are attached to Y-legs. The front face of the edge of the mirror is pushed up from front by a spring plunger inside each knuckle. From behind, we have three fine-threaded (0.7mm pitch size) adjuster screws with hexagonal heads pushing the mirror down. Next to each adjuster screw, there is a clamping screw so that once the alignment is completed, it can be tightened down to fix the camera mirror in position. Since the camera system is inside the cryostat, we have a special cryostat cover that has three feed-through with hex-keys attached so that one can adjust the camera mirror screws from outside when the camera system is in vacuum and cold. Each hex-key has a rotation knob with a dial indicator glued (see F in Figure 4 and Figure 5). The indicator has 1-degree division mark with a diagonal line at every 45 degrees. A knife-edge blade is attached to the indicator. This allows us to rotate the knob to place a desired division mark to the edge of the blade, thus permitting a theoretical resolution of 1/360 turn
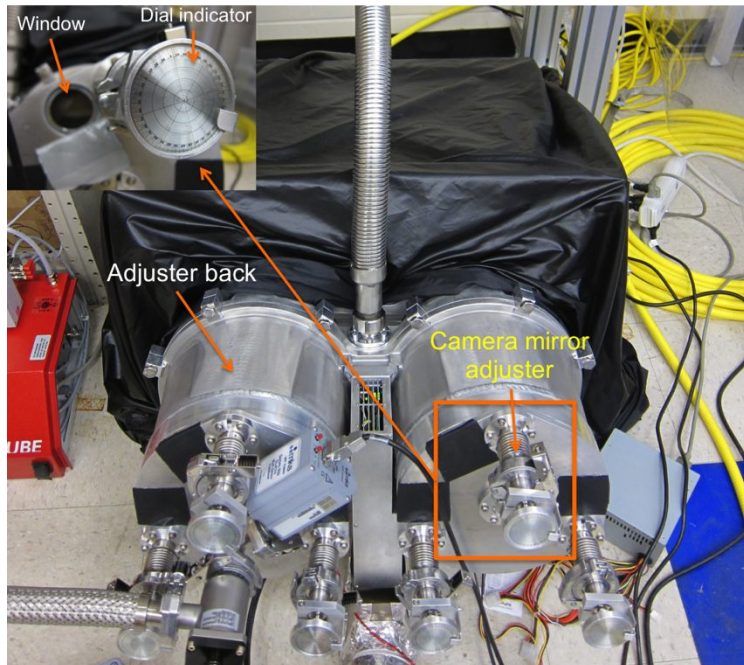
Figure 5 VIRUS unit spectrograph with the camera mirror adjuster back attached for fine alignment.

(i.e. ±2μm in focus motion and ±3arc-seconds in tip/tilt motion). Our experience with these adjusters so far indicates that the repeatability is close to 1/120 turn in peak-to-valley due to backlash. This corresponds to ±6μm in focus and ±9arc-seconds in tip/tilt motion, but is better than the focus requirement of ±10μm and within the tip/tilt requirement of ±10arc-seconds.

Using the camera mirror adjustment, we are able to modulate the focus aberration to the accuracy of ±0.15 wave (at 632.8nm) in peak-to-valley. Our experience indicates that a half turn (0.35mm in the camera focus) is the appropriate amount of maximum modulation and 5 modulations (at 0, ±1/4, ±1/2 turns) are sufficient to determine the first 15 aberration modes of the spectrograph system since the optical components are expected to have negligible aberration modes higher than order 15 based on the interferometry / profilometry measurements of individual surfaces. The higher-order terms of the design itself are removed through our anti-aliasing process. The required turns in fact match the diagonal lines in the indicator, making the focus modulation convenient and accurate.
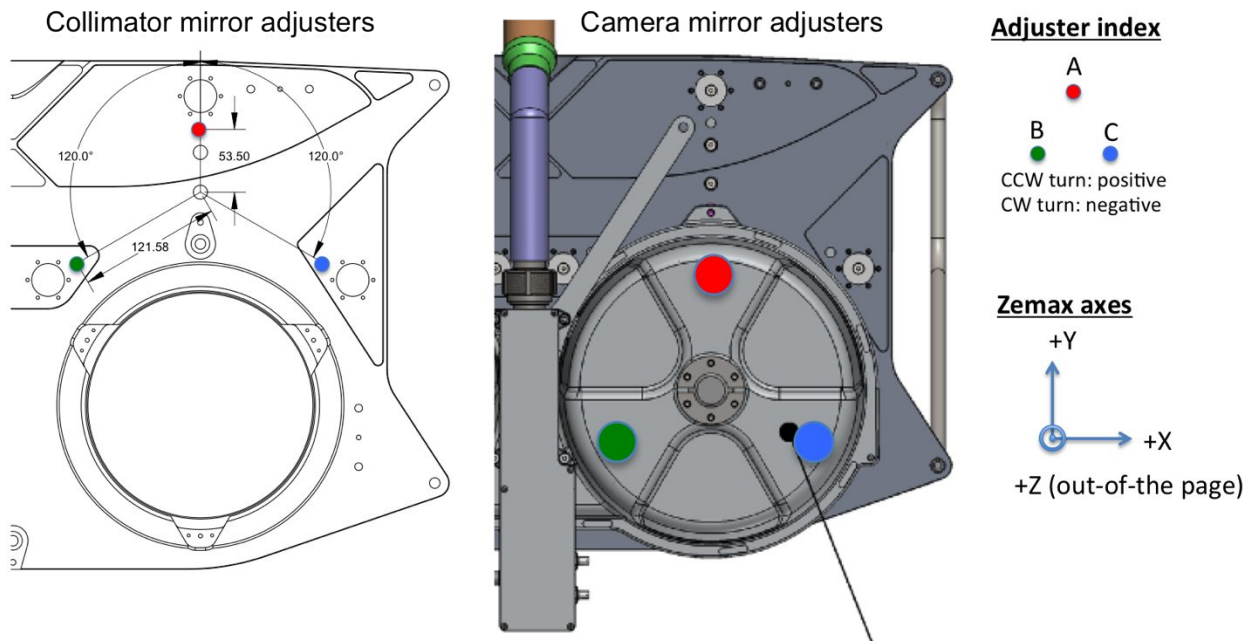
Figure 6 (Left) The locations of the collimator adjusters on the head plate. (Middle) The locations of the camera mirror adjusters on the custom-made cryostat. (Right) The adjuster index, signs for adjuster turn direction, and the definition of the Zemax coordinate axes used in the alignment.

Figure 6 shows the locations of the collimator and camera mirror adjusters. The adjuster indexes and coordinate axes are also shown. In order to calculate the required number of turns of each adjuster for desired amounts of tip/tilt/focus motions of the collimator and/or camera mirror, we derived the following matrix equations.

$$\begin{bmatrix} N_A \\ N_B \\ N_C \end{bmatrix} = \frac{3R}{\delta} \begin{bmatrix} \frac{1}{3} & 0 & \frac{1}{3R} \\ -\frac{1}{6} & \frac{1}{2\sqrt{3}} & \frac{1}{3R} \\ -\frac{1}{6} & -\frac{1}{2\sqrt{3}} & \frac{1}{3R} \end{bmatrix} \begin{bmatrix} \Theta_x \\ \Theta_y \\ Z \end{bmatrix} \text{ and } \begin{bmatrix} N_A \\ N_B \\ N_C \end{bmatrix} = \frac{2}{\delta Q} \begin{bmatrix} R_1 + d_1 & 0 & 0 \\ 0 & R_2 + d_1 & 0 \\ 0 & 0 & R_2 + d_1 \end{bmatrix} \begin{bmatrix} d_1\sqrt{3} & 0 & \frac{\sqrt{3}}{2} \\ -\frac{d_2\sqrt{3}}{2} & d_1 + \frac{d_2}{2} & \frac{\sqrt{3}}{2} \\ -\frac{d_2\sqrt{3}}{2} & -\left(d_1 + \frac{d_2}{2}\right) & \frac{\sqrt{3}}{2} \end{bmatrix} \begin{bmatrix} \Theta_x \\ \Theta_y \\ Z \end{bmatrix}$$

The left matrix equation is for the camera mirror adjustment and the right is for the collimator adjustment. Θ_x and Θ_y are tilt about X and Y axis, respectively. Z is the focus. R value in the camera mirror equation is the radial location of each adjuster with respect to the center of the camera mirror (or the optical axis of the camera). δ is the pitch size of the adjuster screw. The equation appears a little bit different for the collimator mirror adjustment since the radial location of Adjuster A (R_1) is shorter than that of the other two (R_2). As a result, when Adjuster A is adjusted, the collimator mirror rotation pivot point is not on the same radial location as that of the other two adjusters. Q is $\sqrt{3}(2d_1+d_2)$. Both equations produce the number of turns of each adjuster for the desired mirror tip/tilt/focus values. In fact, the actual relation between these two sets of quantities is non-linear. Therefore, the above equations are just approximations to those. However, when the above equations were used in the Zemax model, we were able to match the actual values to accuracy of 1μm in focus and 0.5 arc-seconds in tip/tilt. This is far better than the required adjustment accuracy.

An example modulation image is shown in Figure 7, showing the fiber core images at discrete emission lines (i.e. the IFU is illuminated by Mercury (Hg) and Cadmium (Cd) emission line lamps) across the CCD (2064×2064 with 15μm pitch). Note that the vertical axis corresponds to the fiber-slit direction and the horizontal axis corresponds to the dispersion direction with the blue end (350nm) being near the left edge of the image. In order to aid the modulation and the IWFS analysis, we made an IFU mask (that has circular openings (250μm +0/-25μm in diameter) for 17 chosen fibers so that each fiber image has enough empty pixels from adjacent fibers in the spatial direction. In addition, the Hg and Cd line sources produce a sufficient number of well-separated lines across the CCD. As shown in the sample modulation image, there are two central fibers close to each other. These two fibers are too close to be used in the IWFS analysis. However, the main purpose of these fibers is to check the location of the spectra with respect to the CCD center. In total, there are 105 available targets across the CCD for the IWFS analysis.
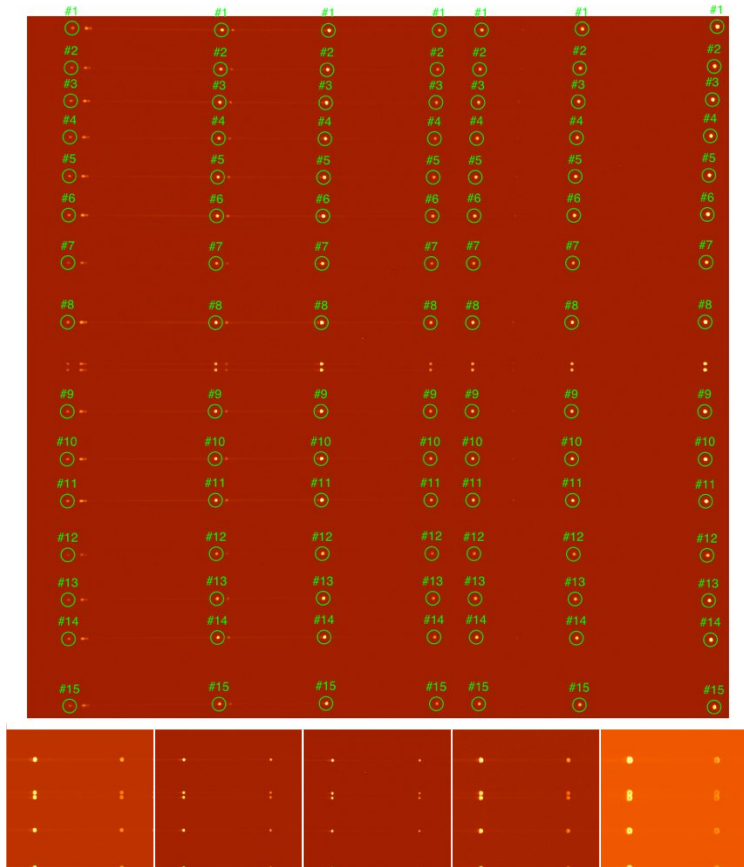

Figure 7 A sample modulation image from the VIRUS unit. (Top) The zero modulation image with fiber target indexes and analysis apertures overlaid. (Bottom) The zoomed-in central sections of 5 modulation images.
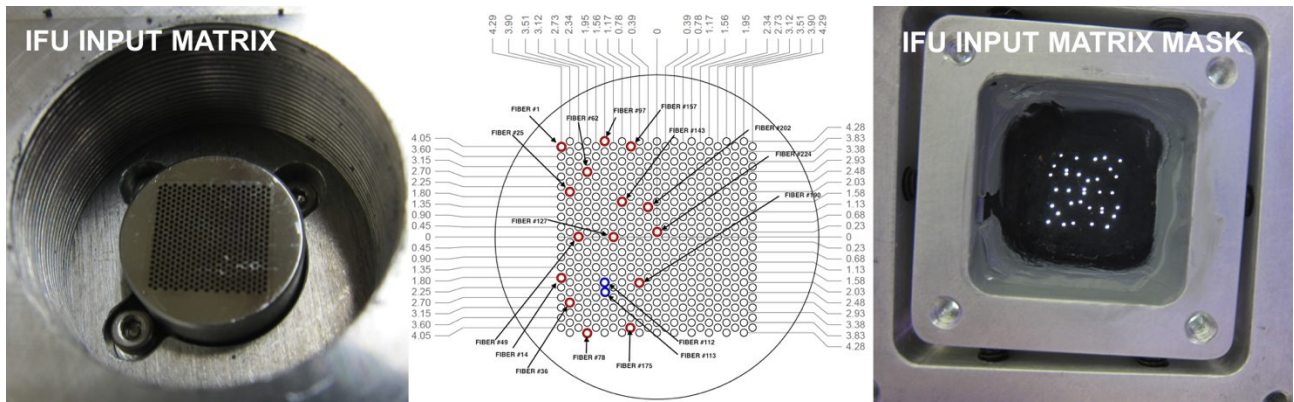
Figure 8 (Left) A snapshot of the IFU input matrix. (Middle) The IFU input matrix layout and the locations of the 17 mask openings marked. (Right) A fabricated IFU input matrix mask.

3.3. Testing the IWFS in Zemax simulation

Before applying the IWFS to the nominal VIRUS unit, we have conducted a test (see additional simulation case studies in Ref. [17]. A set of 5 focus-modulated VIRUS images was simulated in Zemax at 9 different wavelegths and 15 fiber positions on the fiber slit (Figure 9). The images were subjected to photon noise and the VIRUS readout noise (3.1e⁻ rms per pixel). Note that background was not considered because background is subtracted in real image reduction process. Also assumed is that the fibers are illuminated by the same amount of light at all wavelengths (i.e. no fiber-to-fiber variation).
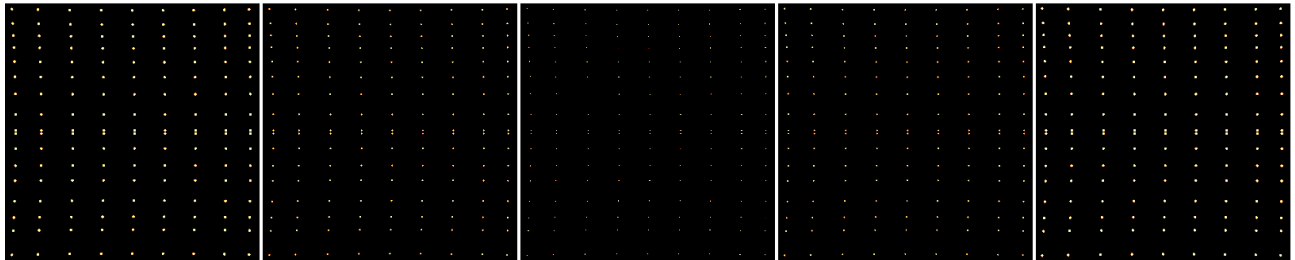
**Figure 9** A set of simulated images from the VIRUS unit Zemax model.
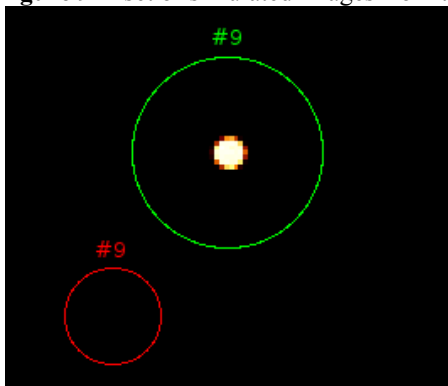
Figure 10 Close-up view of a fiber target with analysis apertures overlaid.

When each fiber target is analyzed, we first create two apertures as shown in Figure 10. The first aperture (i.e. the larger aperture with green color) is the target analysis aperture. This is the place where the image moments of the target fiber are computed. The aperture is slightly oversized so that it can enclose the target at all focus modulations. The second aperture (i.e. the smaller aperture with red color) is the background analysis aperture. Within this aperture, we compute the background and readout noise that are used in the analysis of the target fiber.

Once the background aperture analysis is completed, the data are used to estimate the error in computing image moments of the target fiber. In addition, the target fiber shape profile is also computed to determine the contribution of pixilation to the moment measurement error. If the modulation accuracy is known, this value is also used to determine the contribution of the modulation uncertainty to the total moment measurement error. One of the potential error sources is the higher-order aliasing. Since we are estimating the first 15 aberration modes, if there exits a strong higher-order modes beyond order 15, these un-sensed strong higher-order modes spills its power into their lower order counter parts. The as-designed VIRUS unit does not show significant higher order modes beyond order 15, but we computed the higher-order modes from order 15 up to 37 and then calculated their contribution to the first 15 modes. This contribution is then later subtracted out from the aberration

values determined by the IWFS so that the mode values are free from the aliasing. This procedure is called 'anti-aliasing'. All these error values are combined and then propagated through the rest of the analysis procedure (i.e. determining the moment derivatives, computing the slope aberration from the derivatives, and then calculating the wave aberrations from the slope aberrations). Detailed error propagation will be treated in a separate report. For the parameters used in the simulations, the estimated wavefront coefficient error is within ±1/10 wave in peak-to-peak. This applies to the results shown below.

Some of the comparison results are shown in Figure 11. The top-left plot shows the RMS wavefront error (WFE) at the wavelength of 375nm across the fiber slit. The blue curve shows the RMS WFE values calculated from applying the IWFS to the simulated images. The red curve is from the Zemax standard Zernike coefficient calculation. The IWFS curve very closely follows the Zemax curve. The maximum deviation from the Zemax curve is less than 1/20wave at the edge of the fiber slit. On the bottom-left panel, we have a plot of the focus aberration at the same wavelength across the fiber slit. The IWFS curve closely follows the Zemax curve. The maximum deviation occurs at the edge of the slit and the amount is 1/13 wave. The top-right panel shows the 45-deg astigmatism at 425nm across the fiber slit. It shows a cubic variation that very closely matches the Zemax calculation. The maximum variation occurs at the top of the fiber slit (<1/20 wave). The bottom-right panel shows the spherical aberration at the wavelength of 525nm across the fiber slit. Again the IWFS result closely matches the computation from Zemax. Note that the VIRUS unit Zemax model has all central obscuration components that are field-dependent. Therefore both IWFS and the Zemax calculation were subjected to these obscurations. Since the IWFS computation assumes a filled circular pupil, the estimated values are not truly orthogonal mode coefficients. At the same time, the Zemax aberration coefficients were also affected by the obscuration and therefore not orthogonal either. Therefore, this test result illustrates that the IWFS matches the Zemax results in the same circumstance.
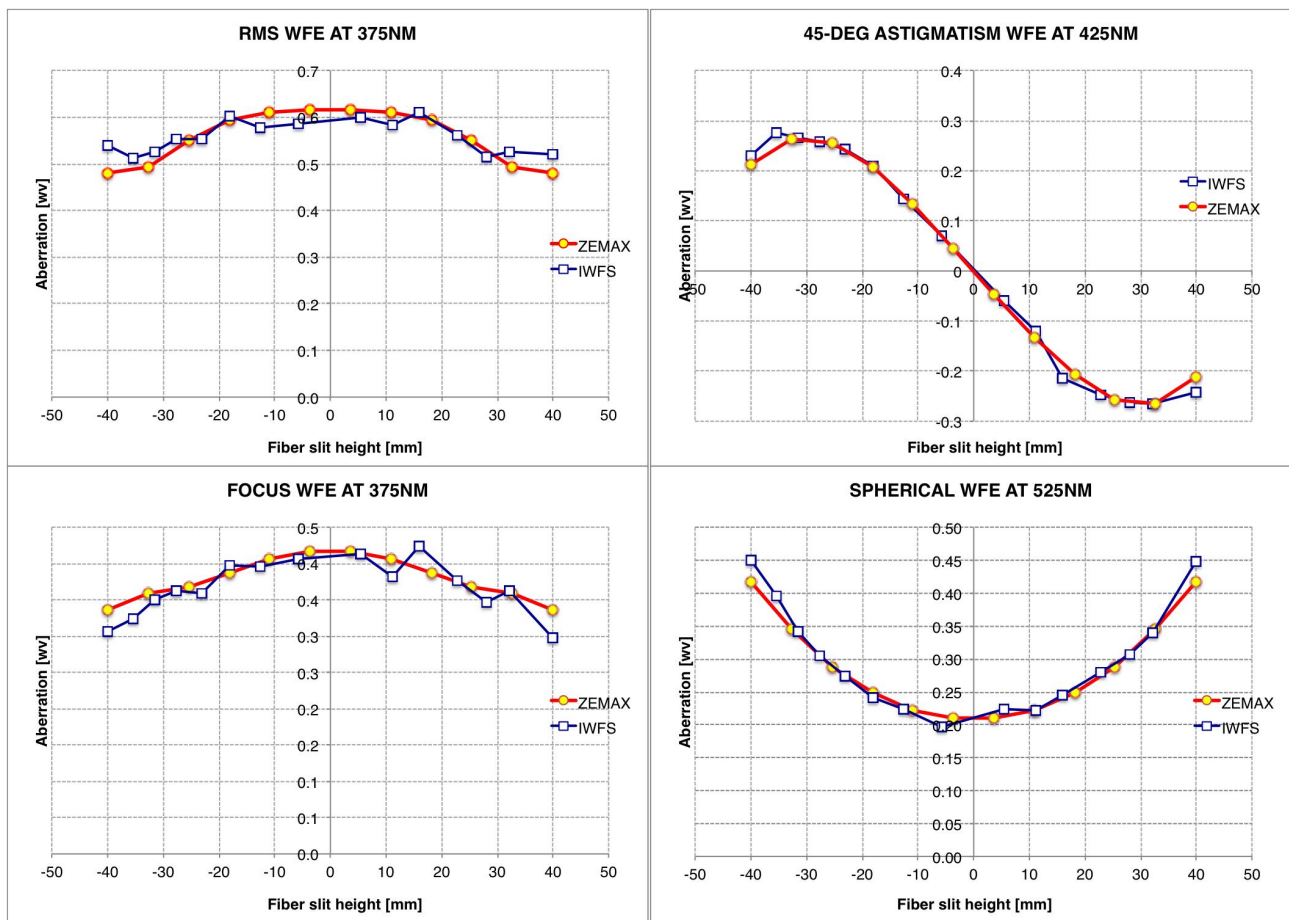
Figure 11 Comparisons of the aberration values from Zemax's ray-tracing-based aberration coefficient calculation.

3.4. Application of the IWFS to the fine optical alignment of the VIRUS unit.

We applied the presented modal sensing technique to the VIRUS unit. The modulated images are passed through a basic reduction pipeline to remove the back ground images, to write appropriate fits header information, and then to adjust the image format since the CCD generates two frames with over-scan areas around them so it is necessary to remove these over-scan areas to properly register one frame to the other. The moment analysis program as used in the previous test analyzes the reduced images and produces the first 15 aberration modes. Since the individual optical components are made to the specification, the main interest is to sense any gradient in the low order aberration modes due to misalignment. One example is shown in Figure 12. The top-left plot shows the determined focus aberration across the fiber slit at 7 different wavelengths. It shows a strong focus gradient in the system, amounting 10 wave in peak-to-valley from one end of the slit to the other. The curves are systematically offset by 1 wave. The slope of the curves tells the amount and the direction of the tilt correct needed for the camera mirror. Once the correction is applied, the curves become flat as shown in the top-right plot. There is a small amount of gradient in the direction of the wavelength, which is negligible thus not corrected. The image quality of the system also reflects this as shown in the bottom plots. Due to the linear focus gradient, the image quality (i.e. full-width at half-maximum of a point spread function) shows a quadratic variation across the fiber slit (Bottom-left). After the tilt correction, the image quality becomes flat as shown in the bottom-right plot. The estimated error of each focus value is ±1/10 wave. The error of each FWHM estimate is ±0.15 pixel in rms.
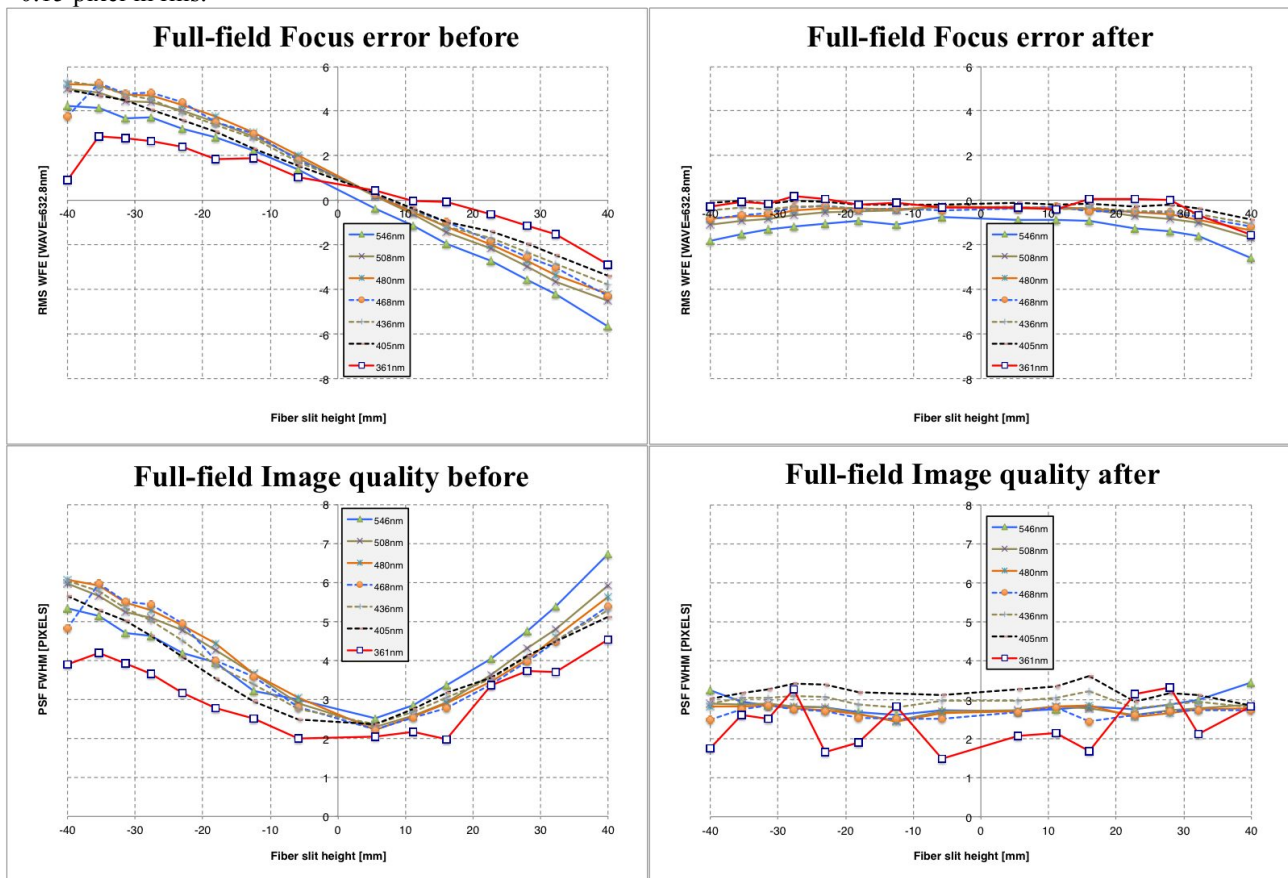
Figure 12 Example analysis results from the moment-based modal sensing of the VIRUS unit spectrograph. Each curve is plotted across the fiber slit at a particular wavelength. (Top-left) Focus aberration across the CCD before correction. (Top-right) Focus aberration across the CCD after correction. (Bottom-left) PSF FWHM before correction and (Bottom-right) after correction.

An interesting comparison is shown in Figure 13. Here we derived the edge spread function (ESF) of the fiber image (at fiber slit location of 3.95mm and wavelength of 436nm). The left panel shows the central section of the image at its

zero modulation. The panel next to it shows the close-up view of the target fiber used to compute the ESF. Also shown to the right is a vertical slice profile of the fiber image. The right panel shows the ESF derived by computing the derivative of the vertical profile. The ESF is marked by 'ESF' in the plot. The plot shows two ESFs, but the left one is the true ESF since there is an empty area below the bottom fiber and thus the profile is the true representation of the ESF. The computed FWHM value of the ESF is 2.93 pixels with uncertainty of ±0.29pixels. In the IWFS result, we actually computed the FWHM value for the fiber image close to this location (see points near the center at wavelength 436nm in the bottom-right picture of Figure 12). The IWFS' FWHM value is 2.97 pixels with uncertainty of ±0.1pixels. The FWHM derived from the ESF in fact confirms the value derived from the IWFS analysis.
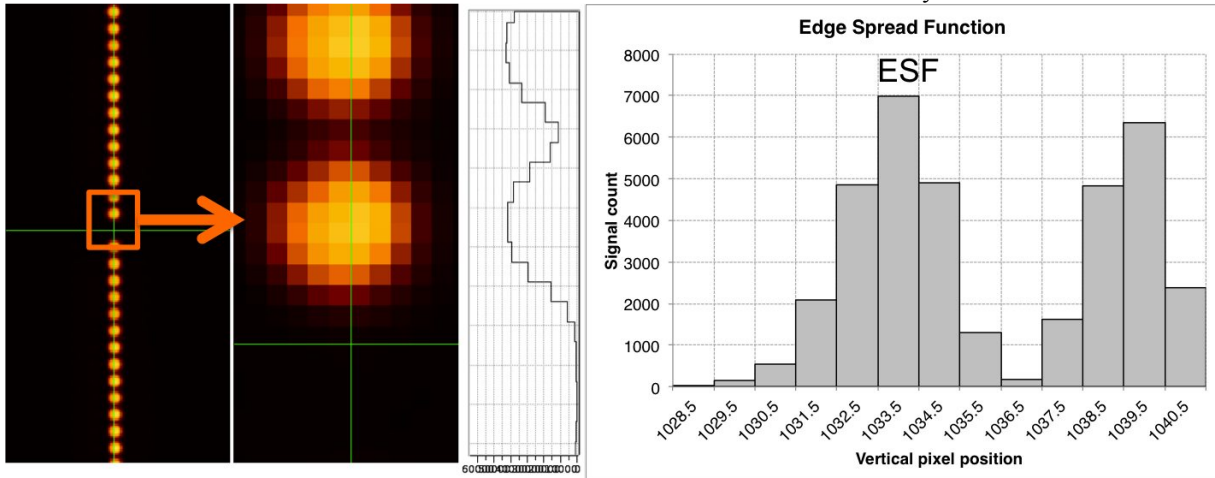
Figure 13 The edge spread function (ESF) computed from the zero modulation image (fiber slit location: 3.95mm, wavelength: 436nm). (Left) The section view of the fiber image and its close-up view with a vertical slice profile plotted. (Right) The ESF computed by taking the derivative of the edge profile of the bottom fiber image.

Another example is shown in Figure 14 where focus is expressed in terms of the actual focus error (i.e. the axial distance of the optimum focus from the current focus). The top-left panel shows the initial gradient amounting to 160μm across the CCD (not fiber slit). The fiber images of the initial alignment state are shown in the bottom left panel. In the middle panel, an example set of 5 focus-modulated fiber images is shown. Based on the focus gradient measurement, the camera mirror was tilted in the spatial direction and the top-right plot shows the focus measurement across the CCD. The curves are flattened out. The improvement is directly reflected in the same fiber images shown in the bottom-right.
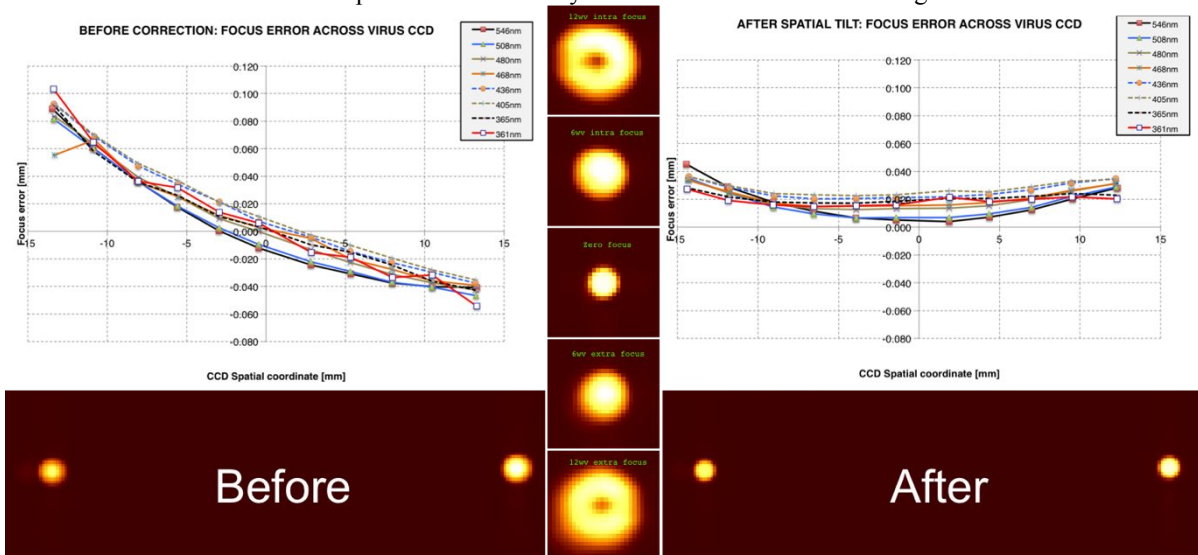
Figure 14 Fine optical alignment example, (Left) Initial focus error, (Middle) Focus modulation images, (Right) Focus error after correction

Our experience indicates that the IWFS analysis for the 105 fiber targets over 5 focus-modulated images takes about 2 minutes on a Apple MacBook Pro laptop computer (2GHz Intel core i7 processors with 8GB DDR 3 RAM). The actual data acquisition takes about 5 minutes per modulation when taking multiple (5) target images and (5) background images with exposure as long as 5 seconds for the maximum focus modulation. The read-out time per image is 13seconds. It takes about less than 1 minute to change the modulation using the camera adjusters.

4. SUMMARY

A new concept of using focus-diverse point spread functions (PSF) for modal wavefront sensing (WFS) is presented. This is based on relatively straightforward image moment analysis of measured PSFs, which differentiates it from other focal-plane WFS (FP-WFS) techniques. The presented geometric analysis shows that the image moments are nonlinear functions of wave aberration coefficients but notes that focus diversity essentially decouples the coefficients of interest from others, resulting in a set of linear equations whose solution corresponds to modal coefficient estimates. The presented the application of the IWFS fine optical alignment using to in-situ full-field image quality analysis of a real spectroscopic system (the VIRUS unit spectrograph). The result demonstrates that the IWFS works in practice can be used as an image quality/alignment analysis tool for various imaging and spectroscopic systems..

ACKNOWLEDGEMENTS

REFERENCES

[1] John W. Hardy, Adaptive Optics for Astronomical Telescopes (Oxford, 1998).
[2] F. Roddier, "Curvature sensing and compensation: a new concept in adaptive optics, " Appl. Opt. 27, 1223 – 1225 (1988).
[3] James R. Fineup, "Phase retrieval algorithms: a comparison," Appl. Opt. 21, 2758 – 2769 (1982).
[4] J. Dolne, P. Menicucci, D. Miccolis, K. Widen, H. Seiden, F. Vachss, and H. Schall, "Advanced image processing and wavefront sensing with real-time phase diversity," Appl. Opt. 48, A30 (2009).
[5] R. Gonsalves, "Small-phase solution to the phase-retrieval problem," Opt. Lett. 26, 684 (2001).
[6] S. Meimon, T. Fusco, and L. Mugnier, "LIFT: a focal-plane wavefront sensor for real-time low-order sensing on faint sources," Opt. Lett. 35, 3036 (2010).
[7] Hanshin Lee, "Modal analysis of focus-diverse point spread functions for modal wavefront sensing of uniformly illuminated circular-pupil systems," Optics Letters 36, 1503-1505 (2011).
[8] G.J. Hill, M.E. Cornell, D.L. DePoy, N. Drory, M.H. Fabricius, A. Kelz, H. Lee, J.L. Marshall, J.D. Murphy, T. Prochaska, S.E. Tuttle, B.L. Vattiat, R.D. Allen, G. Blanc, T.S. Chonis, K. Gebhardt, J.M. Good, D.M. Haynes, P.J. MacQueen, M.D. Rafal, M.M. Roth, R.D. Savage, J.M. Snigula," VIRUS: production of a massively replicated fiber integral field spectrograph for the upgraded Hobby-Eberly Telescope," Proc. SPIE, 8446-21 (2012).
[9] R. Noll, "Zernike polynomials and atmospheric turbulence," J. Opt. Soc. Am. 66, 207-211 (1976).
[10] G.J. Hill, J.A. Booth, M.E. Cornell, J.M. Good, K. Gebhardt, H.J. Kriel, H. Lee, R. Leck, P.J. MacQueen, D.M. Perry, M.D. Rafal, T.H. Rafferty, C. Ramiller, R.D. Savage, C.A. Taylor III, B.L. Vattiat, L.W. Ramsey, J.H. Beno, T.A. Beets, J.D. Esguerra, M. Haueser, R.J. Hayes, J.T. Heisler, I.M. Soukup, J.J. Zierer, Jr., M.S. Worthington, N.T. Mollison, D.R. Wardell, G.A. Wedeking, "Current status of the Hobby-Eberly Telescope wide field upgrade," Proc. SPIE, **8444**-19 (2012).
[11] J. H. Burge, S. D. Benjamin, M. B. Dubin, S. M. Manuel, M. J. Novak, Chang Jin Oh, M. J. Valente, C. Zhao, J. A. Booth, J. M. Good, G. J. Hill, H. Lee, P. J. MacQueen, M. D. Rafal, R. D. Savage, M. P. Smith, B. L. Vattiat, "Development of a wide-field spherical aberration corrector for the Hobby Eberly Telescope", Proc. SPIE, **7733**-51 (2010).

[12]   G.J. Hill, P.J. MacQueen, C. Tejada, P.J. Cobos, P. Palunas, K. Gebhardt, & N. Drory, "VIRUS: a massively replicated IFU spectrograph for HET," *Proc. SPIE*, **5492**, 25, 2004

[13]   G.J. Hill, P.J. MacQueen, P. Palunas, A. Kelz, M.M. Roth, K. Gebhardt, & F. Grupp, "VIRUS: a hugely replicated integral field spectrograph for HETDEX", *New Astronomy Reviews*, **50**, 378, 2006

[14]   G.J. Hill, P.J. MacQueen, J.R. Tufts, A. Kelz, M.M. Roth, W. Altmann, P. Segura, M. Smith, K. Gebhardt, & P. Palunas, "VIRUS: a massively-replicated IFU spectrograph for HET," *Proc. SPIE*, **6269**, paper 6269-93, 2006

[15]   G.J. Hill, P.J. MacQueen, M.P. Smith, J.R. Tufts, M.M. Roth, A. Kelz, J. J. Adams, N. Drory, S.I. Barnes, G.A.Blanc, J.D. Murphy, K. Gebhardt, W. Altmann, G.L. Wesley, P.R. Segura, J.M. Good, J.A. Booth, S.-M. Bauer, J.A. Goertz, R.D. Edmonston, C.P. Wilkinson, "Design, construction, and performance of VIRUS-P: the prototype of a highly replicated integral-field spectrograph for HET", *Proc. SPIE*, **7014**-257, 2008

[16]   S.E. Tuttle, R.D. Allen, T.S. Chonis, M.E. Cornell, D.L. DePoy, G.J. Hill, H. Lee, J.L. Marshall, T. Prochaska, M.D. Rafal, R.D. Savage, B.L. Vattiat, "Initial results from VIRUS production spectrographs," Proc. SPIE, **8446**-221 (2012).

[17]   H.Lee, G.J. Hill, "Image moment-based wavefront sensing for in-situ full-field image quality assessment," Proc. SPIE, 8450-191 (2012).